Nanoscale

PAPER

View Article Online
View Journal | View Issue

Cite this: *Nanoscale*, 2018, **10**, 13011

Magnetism of new metastable cobalt-nitride compounds†

Balamurugan Balasubramanian,*[a,b] Xin Zhao,[c,d] Shah R. Valloppilly,[a] Sumit Beniwal,[a,b] Ralph Skomski,[a,b] Anandakumar Sarella,[a] Yunlong Jin,[a,b] Xingzhong Li,[a] Xiaoshan Xu,[a,b] Huibo Cao,[e] Haohan Wang,[a,b] Axel Enders,[f] Cai-Zhuang Wang,[c,d] Kai-Ming Ho[c,d] and David J. Sellmyer*[a,b]

Received 13th March 2018,
Accepted 27th May 2018

DOI: 10.1039/c8nr02105h

rsc.li/nanoscale

The search for new magnetic materials with high magnetization and magnetocrystalline anisotropy is important for a wide range of applications including information and energy processing. There is only a limited number of naturally occurring magnetic compounds that are suitable. This situation stimulates an exploration of new phases that occur far from thermal-equilibrium conditions, but their stabilization is generally inhibited due to high positive formation energies. Here a nanocluster-deposition method has enabled the discovery of a set of new non-equilibrium Co–N intermetallic compounds. The experimental search was assisted by computational methods including adaptive-genetic-algorithm and electronic-structure calculations. Conventional wisdom is that the interstitial or substitutional solubility of N in Co is much lower than that in Fe and that N in Co in equilibrium alloys does not produce materials with significant magnetization and anisotropy. By contrast, our experiments identify new Co–N compounds with favorable magnetic properties including hexagonal Co_3N nanoparticles with a high saturation magnetic polarization (J_s = 1.28 T or 12.8 kG) and an appreciable uniaxial magnetocrystalline anisotropy (K_1 = 1.01 MJ m^{-3} or 10.1 Mergs per cm^3). This research provides a pathway for uncovering new magnetic compounds with computational efficiency beyond the existing materials database, which is significant for future technologies.

1. Introduction

New materials discovery has governed the development of science and technology for decades.[1–4] Many of the most important magnetic materials were discovered through enlightened solid-state chemistry and intermetallic-compound research.[5–7] This approach often has been focused on Fe or Co-based compounds, since Fe and/or Co are required to achieve high saturation magnetic polarization J_s ($J_s = 4\pi M_s$, where M_s is the saturation magnetization) and Curie temperature (T_c). Magnetic anisotropy is another key intrinsic property, essential to develop coercivity ($B_c = \mu_0 H_c$) in magnetic materials or thermal stability in nanomagnets. Magnetocrystalline anisotropy is a combined effect of spin–orbit coupling and crystal-field interactions and often requires rare-earth or expensive elements.[8] In contrast to the earlier methods, there are three relatively unexplored approaches to the problem of new magnetic-materials discovery. These include: (i) production of new structures by incorporation of gases such as nitrogen, (ii) the use of non-equilibrium methods to generate novel structures, and (iii) the use of high-speed computational methods stimulated by the materials genome initiative. In this research, we combine uniquely all of these approaches to achieve promising magnetic properties in Co–N compounds.

Considering the above-mentioned three approaches separately, it has been shown that the interstitial modification of N can improve the M_s, K_1, and T_c values of Fe-rich magnetic materials such as $Fe_{16}N_2$ and $Sm_2Fe_{17}N_3$.[9,10] Some stoichiometric Co–N interstitial compounds have been reported such as Co_3N and Co_2N, but these exhibit poor magnetic properties.[11–13] An example is the hexagonal compound Co_3N, which crystallizes in the well-known ε-Fe_3N structure (space group $P6_322$) but exhibits a low magnetization (about

[a]Nebraska Center for Materials and Nanoscience, University of Nebraska, Lincoln, NE-68588, USA. E-mail: bbalasubramanian2@unl.edu, dsellmyer@unl.edu
[b]Department of Physics and Astronomy, University of Nebraska, Lincoln, NE-68588, USA
[c]Ames Laboratory, US Department of Energy, Ames, Iowa 50011, USA
[d]Department of Physics and Astronomy, Iowa State University, Ames, Iowa 50011, USA
[e]Quantum Condensed Matter Division, Oak Ridge National Lab, Oak Ridge, TN 37831, USA
[f]Physikalisches Institut, Universität Bayreuth, 95440 Bayreuth, Germany

†Electronic supplementary information (ESI) available. See DOI: 10.1039/c8nr02105h

31 kA m^{-1} or emu cm^{-3}) at 5 K.[11] The second approach, that of non-equilibrium processing, has focused on techniques such as sputtering and rapid quenching from the melt. These methods have produced interesting examples of magnetic compounds such as Co_3Si by sputtering[14] and of $TbCu_7$ and $ThMn_{12}$-type structures by rapid quenching.[15–17] Finally, theoretical and computational tools for new materials discovery have seen significant development in recent years. First-principle calculations and machine-learning techniques show much potential for high-throughput computational materials design. Ideally, this approach can accelerate the discovery of new materials with high efficiency and speed by guiding synthesis methods on the composition and structure of new compounds. Several reviews of advances in this rapidly developing field have appeared recently.[18–23]

Transition-metal nitrides form a rich class of compounds with diverse electronic structure and properties. They are relatively unexplored compounds compared to oxides, yet have properties ranging from metallic to semiconducting and with potential applications as ceramics, magnets, catalysis, and others.[24–28] In this communication, we investigate new Co–N compounds by combining experimental and computational methods as follows. First, non-equilibrium cluster deposition[14] is used to produce a set of metastable Co–N compounds in the form of nanoparticles and the structure and magnetic properties of the Co_3N nanoparticles are determined experimentally using various complementary characterization techniques. Nanoparticle syntheses have shown great potential recently for the development of new Co-rich magnetic compounds with high magnetocrystalline anisotropy and magnetization.[14,29–32] We have focused our search on the Co_3N stoichiometry in this study, because earlier experimental observations on Co–N systems suggest the formation of the cubic structure for nitrogen contents $\leq$20 at% and higher nitrogen contents $\geq$30 at% substantially deteriorates the magnetic properties; for example, Co_2N and CoN are Pauli paramagnets.[11–13] Second, an adaptive genetic algorithm (AGA) is used to assist the determination of the crystal structure for the new nitride compounds. This method predicts the crystal structures of unknown phases relatively rapidly and does not require any assumptions on the Bravais lattice, atom basis, or unit-cell dimensions.[33] Third, spin-polarized density-functional theory (DFT) is applied to new structures in order to calculate their electronic structure and understand their magnetic properties.

2. Experimental methods

Our nanoparticle experiments were carried out by cluster deposition using an inert-gas condensation.[14] In this method, which produces highly monodisperse metal and alloy nanoparticles, an atomic Co vapor produced using direct-current plasma sputtering is condensed in a cooled inert-gas atmosphere to form nanoparticles in the gas-aggregation chamber (for more details, see the Experimental section in the ESI S1†). To form Co_3N nanoparticles, we have fed nitrogen gas (N_2) into the gas-aggregation chamber. Stoichiometry and crystal structure were controlled by nitrogen flow rate, deposition pressure, and growth rate. The nanoparticles were then extracted from the gas-aggregation chamber to another chamber for room-temperature deposition on substrates. Dense nanoparticle films were deposited on Si (111) to measure X-ray diffraction (XRD) using a Cu K_α wavelength of about 1.54 Å, neutron diffraction, binding energy of core-level electrons using X-ray photoelectron spectroscopy (XPS), and magnetic properties using superconducting quantum interference device (SQUID) and physical property measurement (PPMS) system. Carbon-coated Cu grids with low nanoparticle coverage were used for transmission-electron microscopy (TEM) measurements.

3. Results and discussion

Fig. 1A shows the experimental XRD patterns for the nanoparticle samples prepared at different N_2 flow rates in standard cubic centimeters per minute (SCCM). Without the addition of N_2 into the gas-aggregation chamber, the sputtered Co atoms aggregate to form pure Co nanoparticles, which exhibit a mixture of hcp and fcc Co phases as indexed in black and green fonts, respectively, in the XRD pattern (black curve in Fig. 1A). At N_2 flow rates of about 25 sccm (red curve) and 30 sccm (blue curve), the XRD patterns of the nanoparticles are different from that of the Co nanoparticles (black curve) and existing equilibrium phases in the Co–N binary phase diagram[34] and indicate the formation of new structures. Higher nitrogen flow-rates cause the nanoparticles to crystallize in zincblende-type cubic CoN, as exemplified by the XRD pattern for 100 sccm (brown curve in Fig. 1A). Crystal structures of the new cobalt nitrides were searched using the adaptive genetic algorithm[28,33] which was developed based on real-space cut-and-paste operations to generate descendent structures.[35] The searches were carried out at zero pressure and zero temperature with energy as the selection criteria to optimize the candidate structures and in addition, we also have used density functional theory (DFT) in order to calculate the magnetization of the predicted compounds (see the ESI S1† for the details of DFT calculations). The calculated Co_3N structures along with their formation energy (ΔH) at standard or equilibrium conditions and saturation magnetization (M_s) are shown in Table 1 of the ESI S1.† Out of several calculated structures, XRD patterns of the nanoparticles prepared at 25 sccm (red curve) and 30 sccm (blue curve) can be indexed with the new hexagonal (space group: $P6_3/mmc$, prototype: $CdMg_3$) and rhombohedral (space group: $R\bar{3}c$) Co_3N structures, respectively. XPS results also show the Co/N atomic ratio for the hexagonal and rhombohedral nanoparticles as 3.3 and 2.8, respectively (discussed later) and the corresponding stoichiometric values will be used while discussing the hexagonal and rhombohedral nanoparticles. While the rhombohedral-type $Co_{2.8}N$ nanoparticles are single-phase, the XRD pattern of the

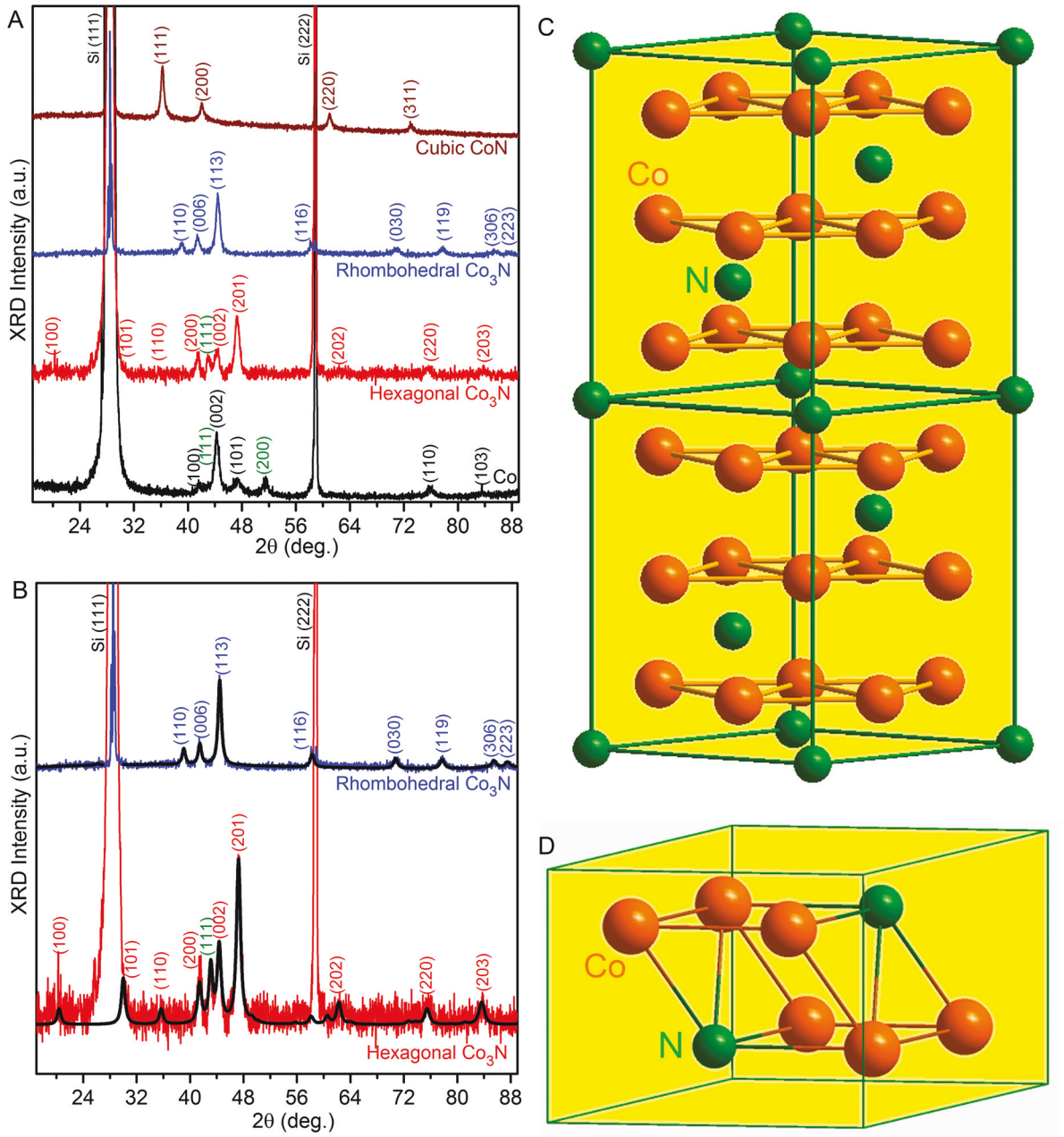

Fig. 1 XRD patterns: (A) The experimental patterns measured using Cu K_α wavelength of about 1.54 Å for the nanoparticles prepared at different N_2 flow rates: Co (0 sccm), hexagonal $Co_{3.3}N$ (25 sccm), rhombohedral $Co_{2.8}N$ (30 sccm), and cubic CoN (100 sccm). (B) The experimental patterns of the hexagonal (red) and rhombohedral (blue) nanoparticles are fitted with the corresponding structures using Rietveld analysis (black curve). New Co_3N structures: (C) rhombohedral and (D) $CdMg_3$-type hexagonal. Brown and green spheres represent Co and N atoms, respectively.

substituted hexagonal $Co_{3.3}N$ nanoparticles exhibits a low-intensity (111) peak corresponding to fcc Co.

We also have performed XRD profile analysis for the nanoparticles using the Rietveld refinement method as shown in Fig. 1B. The experimental XRD patterns of the nanoparticle samples prepared at the nitrogen flow rates of 25 and 30 sccm are in good agreement with the simulated XRD patterns for the hexagonal and rhombohedral-type Co_3N structures, respectively. Rietveld refinement yields a volume fraction of 3% fcc Co, as well as lattice parameters of a = 5.042 Å and c = 4.090 Å (hexagonal phase) and a = 4.611 Å and c = 13.062 Å (rhombohedral).

Note that the rhombohedral structure is an interstitial type and hexagonal Co_3N phase is a substitutional compound. Fig. 1C and D shows the corresponding unit cells. In the rhombohedral structure, the nitrogen atoms forming a sublattice by occupying some of the octahedral interstitial sites in the hcp-Co host lattice. This octahedral interstitial occupancy is the

usual situation for gases in dense-packed metals,[36] and the corresponding theoretical enthalpy of formation, +71.0 meV per atom (Table 1 in the ESI S1†), is moderately high and in a similar range of the calculated formation energy of the known Fe_3N-type hexagonal structure (+72.0 meV per atom). The substituted hexagonal compound crystallizes in the $CdMg_3$-type hexagonal structure. As in the rhombohedral structure, the nitrogen atoms form an ordered sublattice, corresponding to the Cd atoms in the prototype, but the structure is that of hcp cobalt where one fourth of the Co atoms are replaced by nitrogen. This substitution is very unfavorable at thermal equilibrium, with a calculated formation enthalpy of +964.1 meV per atom (Table 1 in the ESI S1†).

As compared to hcp Co and fcc Co, the rhombohedral $Co_{2.8}N$ nanoparticles have several distinct and intense X-ray diffraction peaks at 2θ = 39.12°, 58.32°, 70.89°, 77.79°, 85.23° and 87.58°, corresponding to (110), (116), (030), (119), (306), and (223) reflections, respectively (blue curve in Fig. 1A). On the other hand, it is important during the structural determination of $Co_{3.3}N$ nanoparticles using XRD to properly distinguish between the hcp Co and substituted $CdMg_3$-type structure, which are closely related and have similar XRD patterns. The main difference is the larger unit cell, which means that hcp (h k l) peaks correspond to $CdMg_3$ ($2h$ $2k$ l) peaks. A few distinct XRD peaks at lower angles from (100), (101), and (110) reflections are expected for the $CdMg_3$-type structure, but the intensities of (100) and (110) peaks are small as compared to the intense XRD peaks such as (200), (002), and (201) and the (101) peak is covered by the substrate peak. However, a weak intensity peak corresponding to the (100) reflection of the $CdMg_3$-type structure is visible in the experimental XRD pattern (red curve in Fig. 1A and B). Note that the intensity ratio between the (100) and (200) reflections from the experimental XRD pattern is $I(100)/I(200) \approx 0.58$, comparable with the standard theoretical intensity ratio $I(100)/I(200) = 0.37$ for $Co_{3.3}N$ nanoparticles with the $CdMg_3$-type structure. In support to this result, the analysis of the intensity of the (002) XRD peak and electron diffraction results also indicates that the hexagonal phase is $CdMg_3$, not the crystallographically very similar hcp Co; in addition, X-ray photoelectron spectroscopy (XPS) measurements also show that the stoichiometry is close to Co_3N (see below).

Note that the (002) peak often has been observed to be the most intense XRD peak for hcp Co nanoparticles,[37–41] and this is also true for the pure Co nanoparticles reported in the present study (black curve in Fig. 1A). In contrast, the most intense diffraction peak in the XRD pattern of the hexagonal $Co_{3.3}N$ nanoparticles is (201) as expected for the $CdMg_3$-type structure.

For electron-diffraction measurements, the hexagonal $Co_{3.3}N$ sample with significant amount of particles were deposited on a carbon-coated copper grid and immediately capped with a carbon layer of about 1 nm thickness. Fig. 2A shows the transmission electron microscope (TEM) image of the hexagonal $Co_{3.3}N$ nanoparticles and the corresponding selected area diffraction (SAED) pattern is compared with the simulated electron diffraction pattern of the $CdMg_3$-type structure using a computer program PCED in Fig. 2B.[42] The red-vertical lines marked in Fig. 2B correspond to the simulated intensities of various reflections. As shown in Fig. 2B, the experimental SAED pattern shows good agreement with the simulated diffraction rings corresponding to the $CdMg_3$-type hexagonal structure.

As shown in Fig. 2B, the most intense diffraction pattern is broad due to the combination of (201), (002), and (200) reflections, whose interplanar spacings (d_{hkl}) are 1.905, 2.033, and 2.151 Å, respectively, and close to each other. Outside of these strong reflections, weak diffraction spots corresponding to (200) reflection of the fcc Co are also seen as indicated by an arrow in Fig. 2B. However, the diffraction spots corresponding to the distinct (110), (101), and (100) reflections at higher d_{hkl} values for the $CdMg_3$-type structure are not visible in Fig. 2B due to their low intensities.

As shown in Fig. 2C and D, we also measured SAED pattern at higher magnification in order to focus on the diffraction pattern with larger d_{hkl} values. Several diffractions spots corresponding to the (101) reflection are clearly seen as marked by dotted circles in Fig. 2C and D, and these diffraction spots match with the (101) reflection from the simulated electron diffraction pattern of the $CdMg_3$-type structure as shown in Fig. 2D. We also confirmed that the diffuse diffraction ring observed between the most intense diffraction rings and (101) reflection in Fig. 2C and D is due to the carbon cap layer by measuring the SAED pattern for the carbon layer. If the intensity of the incident electron beam is decreased by adjusting the beam-stopper, a few diffraction spots corresponding to (100) reflection of the $CdMg_3$-type hexagonal Co_3N is also clearly seen (Fig. S1B in the ESI S1†). The observation of (100) and (101) Bragg reflections is a clear evidence of the new $CdMg_3$-type phase that distinguishes it from the structurally related hcp Co.

Note that the d_{hkl} values of the indexed (100) and (101) reflections for the hexagonal nanoparticles using XRD and/or SAED patterns do not match with those standard values of the (hkl) reflections from fcc Co, hcp Co, CoO, cubic nitrides such as CoN and Co_4N or distorted hcp Co_3N, but they show good agreement with the (hkl) reflections of the $CdMg_3$-type structure. In the case of distorted hcp Co_3N, a sizeable increase of lattice parameters ($a \approx 2.66$ Å and $c \approx 4.31$ Å) has been observed as compared to those of hcp Co ($a \approx 2.51$ Å and $c \approx 4.07$ Å), leading to a significant shift of X-ray diffraction peaks of the hcp Co_3N towards lower 2θ values by about 1–2°.[43] Therefore, the positions of XRD peaks of the $CdMg_3$-type hexagonal nanoparticles are significantly different than those of the distorted hcp Co_3N.

The hexagonal and rhombohedral nanoparticles were also deposited on carbon-coated Cu grids with low coverage densities. This is important to avoid the agglomeration of nanoparticles, which helps to measure more precisely their size, size-distribution, and shape. Fig. 3A and B show the TEM images of the substituted hexagonal and interstitial rhombohedral nanoparticles, respectively. The corresponding particle-

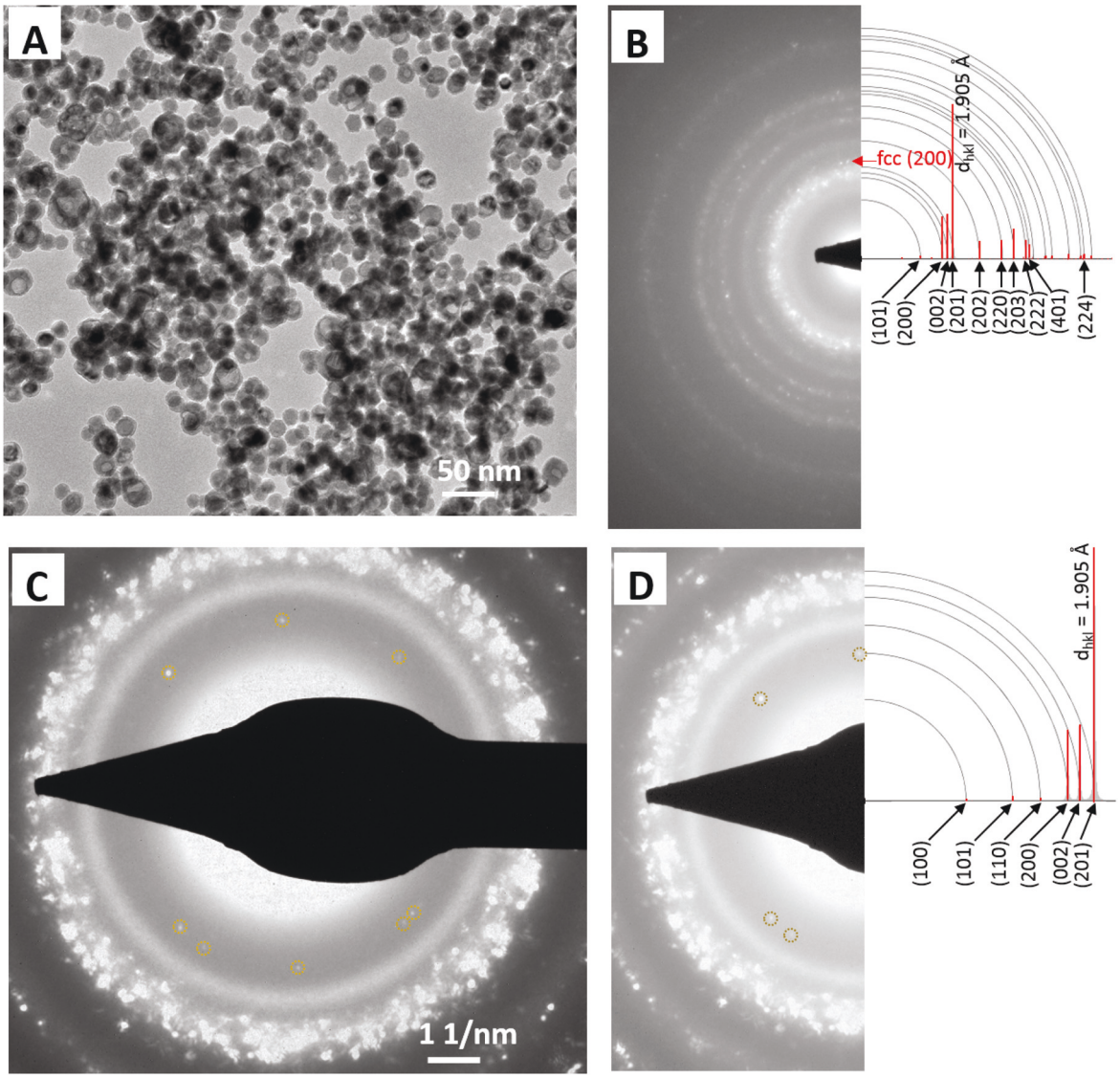

Fig. 2 Electron microscopy results of the hexagonal $Co_{3.3}N$ nanoparticles. (A) TEM image. (B) The experimental selected area electron-diffraction pattern (SAED) is compared with the simulated electron-diffraction pattern of the $CdMg_3$-type structure. (C) SAED pattern at higher magnification, and (D) its comparison with the simulated electron diffraction pattern for the $CdMg_3$-type structure, whereas the diffraction spots corresponding to the (101) reflection are marked by dotted circles. The red-vertical lines in (B) and (D) correspond to the intensity of the simulated diffraction rings. The d_{hkl} value for the most intense diffraction pattern corresponding to the (201) reflection is given as a reference.

size histograms reveal narrow size-distributions with an average particle size d = 16.4 nm and a standard deviation of $\sigma/d \approx 0.07$ for the hexagonal $Co_{3.3}N$ nanoparticles (left inset of Fig. 3A) and d = 14.6 nm and $\sigma/d \approx 0.20$ for the rhombohedral $Co_{2.8}N$ nanoparticles (left inset of Fig. 3B). Note that the $Co_{3.3}N$ nanoparticles of Fig. 3A have facets typical of hexagonal crystal structures, whereas those in Fig. 3B are nearly rhombohedral. High-resolution TEM images of the hexagonal and rhombohedral nanoparticles show good crystalline nature of the nanoparticles as shown in the right insets in Fig. 3A and B, respectively.

In agreement with the X-ray and electron-diffraction studies, XPS results also show a stoichiometry close to Co_3N for the hexagonal Co_3N nanoparticles. For XPS analysis, we have used the areas of Co $2p_{3/2}$ (Fig. 4A) and N 1s peaks (Fig. 4B) as shown in the corresponding core-level XPS spectrum of the hexagonal Co_3N nanoparticles and determined a Co/N ratio of about 3.3. Similarly, the rhombohedral Co_3N nanoparticles show a Co/N atomic ratio of about 2.8. A detailed XPS analysis confirms the existence of chemical bonds between cobalt and nitrogen in both hexagonal $Co_{3.3}N$ and rhombohedral $Co_{2.8}N$ nanoparticles and more details on the XPS measurements, results, and analysis are described in the ESI S2.†

Our structural studies show the formation of hexagonal ($CdMg_3$-type) and rhombohedral nanoparticles. When nanoparticle sizes are on the order of tens of nanometers, it is often found that the nanoparticles adopt the same structures as bulk materials.[44] Thus, our Co_3N nanoparticles with average

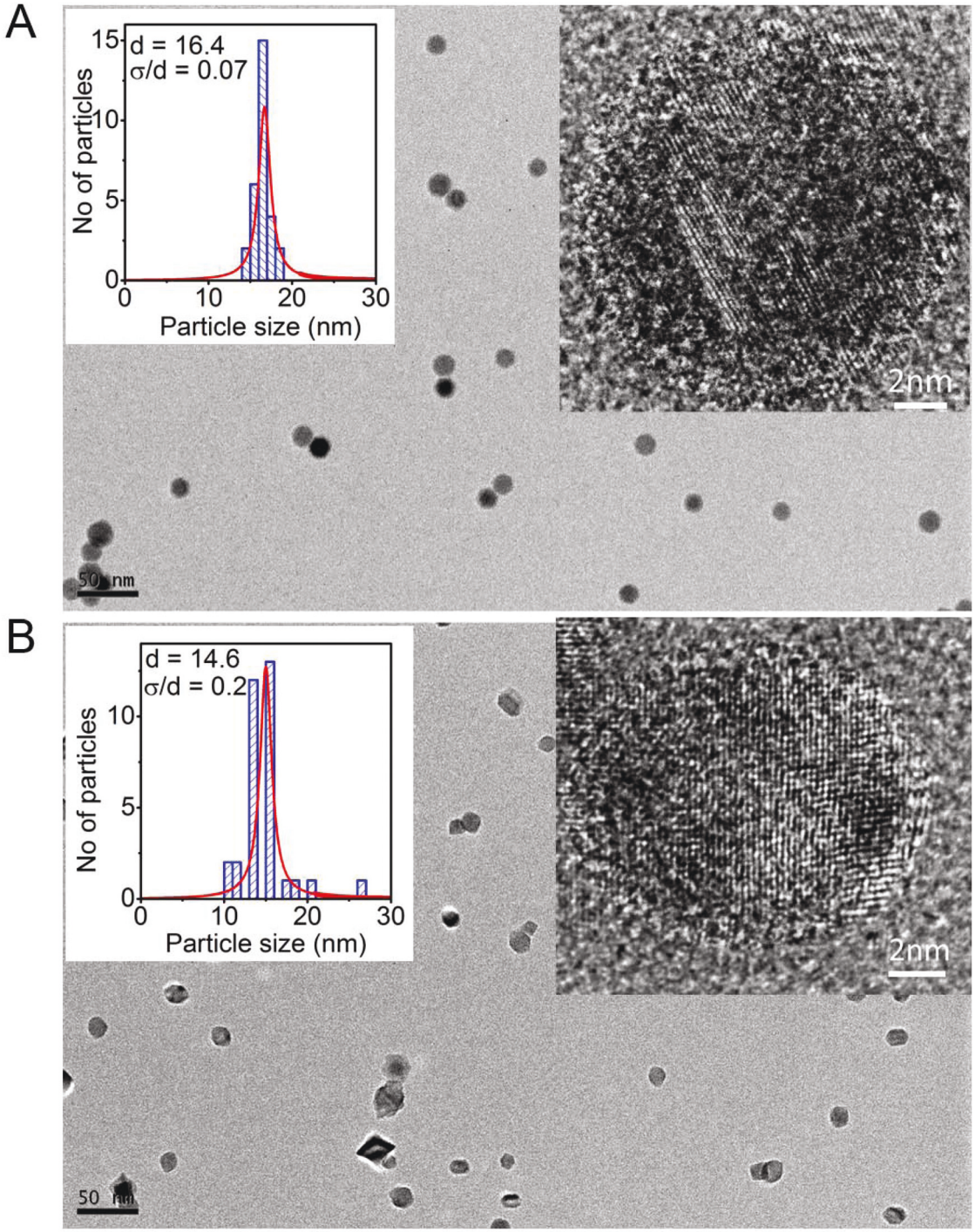

Fig. 3 TEM images for nanoparticle samples. (A) Hexagonal-type $Co_{3.3}N$. (B) Rhombohedral-type $Co_{2.8}N$. The corresponding particle-size histogram (left) and HRTEM image a single particle (left) are shown as insets. σ and d are the standard deviation and average particle size, respectively. The histograms are fitted with Lorentzian distributions (red curves).

sizes of about 14.6 and 16.4 nm are larger enough to be representative of bulk metastable structures. The enthalpy difference of 964.1 meV per atom for the hexagonal structure at equilibrium or standard conditions is large and unusual. Since the high standard formation energy only predicts the phase stability at standard conditions, it does not rule out the formation of Co_3N during the initial stage of the growth in the reactive plasma. It is worth noting that metal nitrides such as MoN_2, Cu_3N, and Na_3N with high formation energy has been fabricated using non-equilibrium synthesis methods.[45–47]

Note that the calculations for energy formation of the Co_3N phases are made at standard conditions using hcp Co and N_2

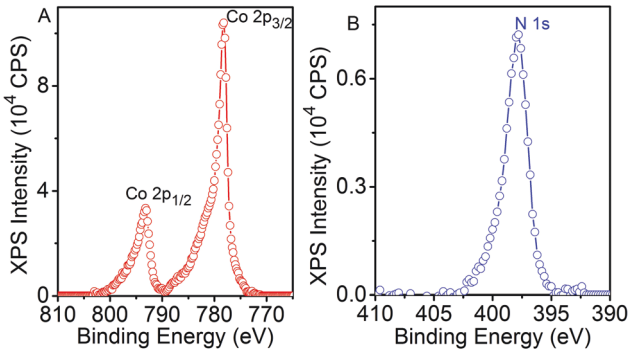

Fig. 4 XPS spectra of the core-level electrons for the hexagonal-type $Co_{3.3}N$ nanoparticles. (a) Co 2p and (b) N 1s.

as references by following $\Delta H(Co_3N) = [E(Co_3N) - 0.5E(N_2) - 3E(Co)]/4$, and thus the energy required to dissociate N_2 is expected to be high.[48] However, our approach uses the non-equilibrium inert-gas-plasma condensation-type cluster-deposition process for the growth of the cobalt nitride nanoparticles, and reactive nitrogen precursor having atomic nitrogen is generally produced by cracking of N_2 molecules in the plasma during the reactive sputtering process,[24] *i.e.* nitrogen atoms are readily available in the plasma to react with Co nanoparticles for forming the Co_3N phases, and this non-equilibrium condition subsequently help to overcome the high formation energy.[24] After the formation, the nitrogen may prefer to leave the nanoparticles but presumably has no time to diffuse to the surface before cooling to room temperature, and thus the $CdMg_3$-type $Co_{3.3}N$ nanoparticles have been observed to be stable while they are brought to room temperature. Similar results also have been observed in other nitride systems. For example, MoN_2 with *R*3*m* structure has shown a high positive formation energy of 819 meV per atom using $Mo + N_2 = MoN_2$.[45] However, this compound has been produced at high pressure of about 3.5 GPa and annealing at 753 K for 20 h.[46] Similarly, the formation energies of Na_3N (+210 meV per atom) and Cu_3N (+260 meV per atom) are high and possitive,[24] but these phases have been grown using reactive plasma synthesis and sputtering, respectively.[47] Like $Co_{3.3}N$, MoN_2, Cu_3N and Na_3N also become stable while they were brought to room temperature and atmospheric pressure.

The calculated saturation magnetizations of bulk rhombohedral and hexagonal Co_3N structures using density functional theory (DFT) are 662 kA m^{-1} (or J_s = 0.83 T) and 1198 kA m^{-1} (or J_s = 1.51 T), respectively (Table 1 in the ESI S1†). The latter value is remarkable and is in the range of values measured for the rare-earth permanent-magnet materials such as $SmCo_5$ (1.01 T), Sm_2Co_{17} (1.2 T), and YCo_5 (1.06 T)[49] and substantially higher than that of the equilibrium Co–N compounds.[11–13] From the corresponding densities of states, we see that the rhombohedral compound is a weak ferromagnet (Fig. 5A), with holes in both the ↑ and ↓ bands, whereas the hexagonal compound is a strong ferromagnet, with essentially a fully occupied ↑ band (Fig. 5B). Fig. 5C shows the hysteresis loops of the substituted $CdMg_3$-type hexagonal nanoparticles at 10 K and at room temperature. There is no significant difference between the saturation magnetization values at the two temperatures, which indicates a high Curie temperature, much above room temperature. The experimental saturation magnetization is 1014 kA m^{-1} at 10 K, which corresponds to a saturation magnetic polarization of J_s = 1.28 T (12.8 kG) and comparable with the theoretical value (M_s = 1198 kA m^{-1} or 1198 emu cm^{-3}). Our DFT calculations are carried out for perfect single crystals, but the experimental samples might have structural features such as subtle compositional and surface in homogeneities or other defects. This could be a possible reason for the slight difference between the experimental and theoretical magnetizations.

The temperature dependence of the nanoparticle magnetization for the $CdMg_3$-type hexagonal structure is shown in Fig. 5D. There is a pronounced magnetization minimum near 600 K, which we interpret as a Curie transition immediately followed by the decomposition of the substitutional phase into N_2 and elemental Co above 615 K. Such decompositions are very common in Co- and Fe-based nitrides[7,12] and, in the present system, supported by XRD and XPS results (ESI S3†). Our results indicate that the hexagonal $Co_{3.3}N$ phase is stable up to at least 600 K (~327 °C) and this is important because permanent-magnet materials are needed for use above room temperature, for example up to 180 °C in high-performance motors.

To study the magnetic transition and phase stability of the hexagonal $Co_{3.3}N$ nanoparticles as discussed above, we carried out neutron diffraction on a thin-film sample composed of easy-axis-aligned hexagonal $Co_{3.3}N$ nanoparticles. The nanoparticles were aligned by applying a magnetic field $B_x = \mu_0 H_x$ = 0.5 T or 5 kG parallel to the substrate during the deposition *i.e.* the field was applied along the *x*-direction with respect to the substrate (see the ESI S4† for details). Fig. 6A compares the out-of-plane (*z*-axis) XRD patterns of the unaligned (isotropic) and aligned nanoparticles. It is clearly seen that the intensity of (002) peak significantly decreases and that of the (200) peak increases in the XRD pattern of the aligned nanoparticles as compared to those corresponding intensities in the XRD pattern of the isotropic nanoparticles. This result indicates that the *c*-axis of the hexagonal Co_3N crystal is the easy direction for magnetization and aligned along the direction of the magnetic field B_x, which is applied along the substrate plane during the deposition. A pole-figure analysis of the (002) peak also shows that the {002} is aligned predominantly along the direction of B_x in the film plane (see the ESI S4† for details).

Generally neutron diffraction consists of nuclear and magnetic contributions. The nuclear diffraction measures the ordering of atoms; it is more sensitive to N than to Co, because the scattering length of N is about 3 times as large as Co.[50] On the other hand, the magnetic diffraction measures the ordering of magnetic moments. The important result is that the temperature dependence of the (002) diffraction intensity show a clear transition between 500 K and 600 K as shown in Fig. 6B, and this transition appears to be reversible

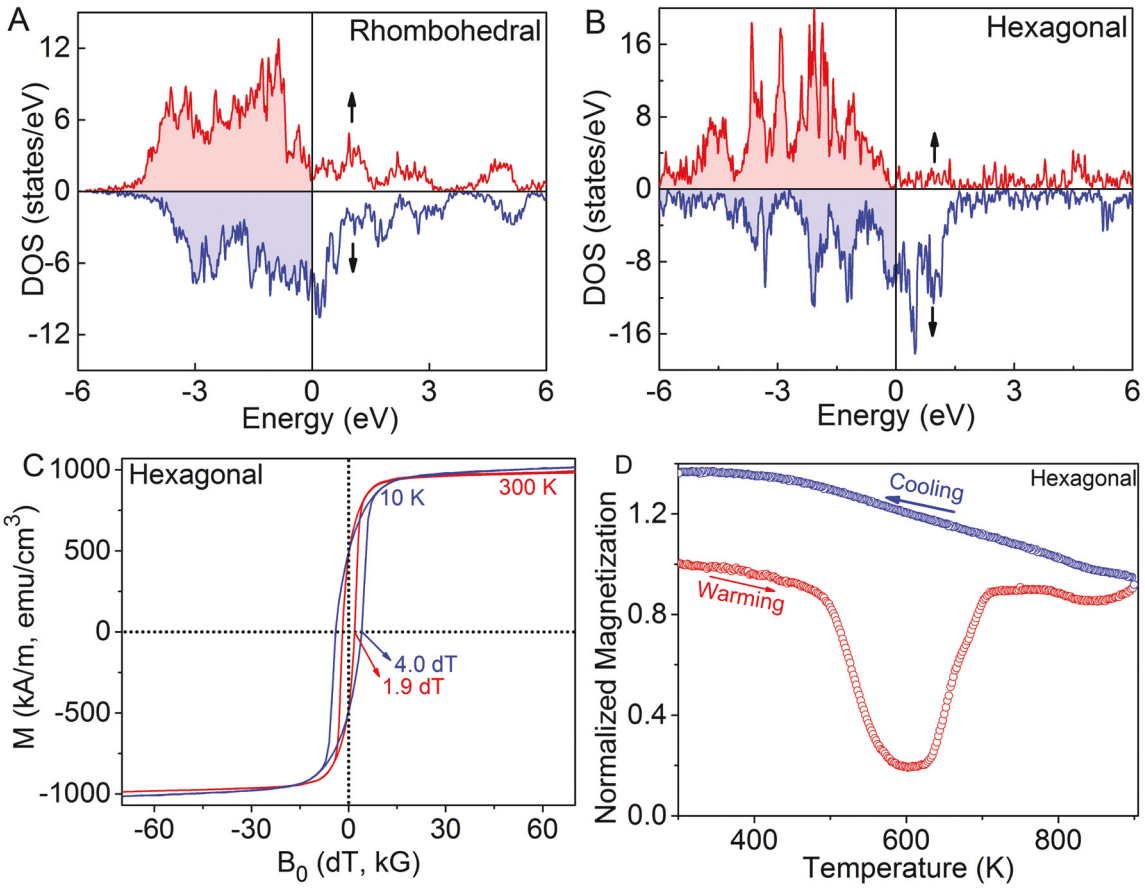

Fig. 5 Magnetic properties: (A), (B) Densities of states for bulk rhombohedral and hexagonal Co_3N structures, respectively. (C) Hysteresis loops measured at 300 K and 10 K for the hexagonal Co_3N nanoparticles as a function of external magnetic field ($B_0 = \mu_0 H$). (D) Magnetization measured as a function of temperature for the hexagonal Co_3N nanoparticles in a magnetic field of 1.0 dT (1.0 kG) during warming (red curve) and cooling (blue curve). The magnetization is normalized with the room-temperature value.

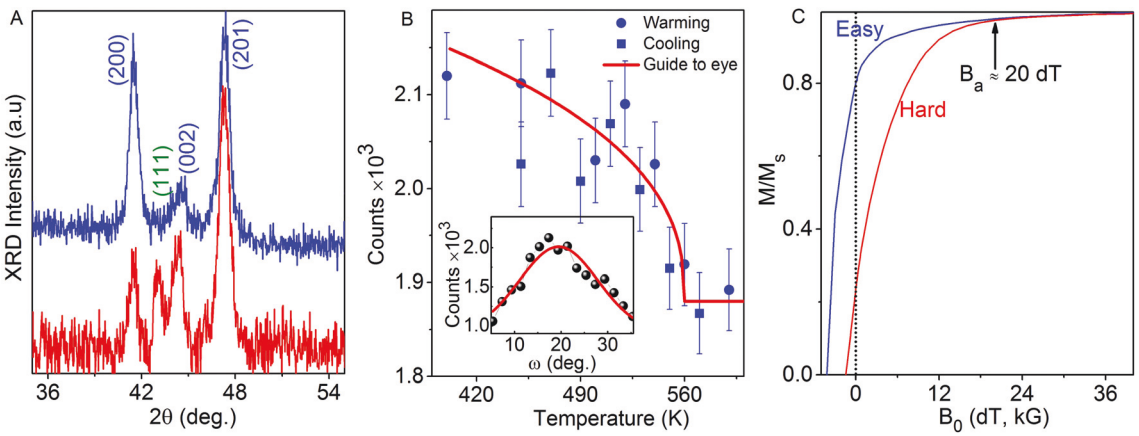

Fig. 6 Easy-axis aligned hexagonal-type $Co_{3.3}N$ nanoparticles: (A) Out-of-plane XRD patterns measured for the unaligned (red curve) and aligned (blue curve) samples. The XRD patterns are indexed to the $CdMg_3$-type hexagonal structure. A weak (111) peak corresponding to the fcc Co is also seen. (B) Neutron diffraction intensity of the (002) peak for the aligned nanoparticle film shows a transition for both warming (circle) and cooling (square) between 500 K and 600 K, whereas the red line is a guide to the eye. The inset shows the rocking curve of the (002) peak, whereas the red line is the Gaussian fit to the data. (C) Magnetic hysteresis loops measured at 10 K along the easy (x) and hard (y) axes. The anisotropy field $B_a = \mu_0 H_a$ is indicated by an arrow.

(warming followed by cooling). Since neutron diffraction is sensitive to N, our result indicates that the structural decomposition of $Co_{3.3}N$ nanoparticles in terms of N loss is minimal up to 600 K. The transition observed between 500 and 600 K in Fig. 6B is consistent with the magnetic transition shown by the temperature-dependent magnetization curve (Fig. 5D). Therefore, there is a sizable magnetic contribution to the neutron diffraction, which suggests a magnetic ordering. The fact that one can observe the magnetic transition in the (002) diffraction indicates non-zero magnetic moment perpendicular to the *c* axis, which could be due to the exchange interaction between the partially aligned particles.[51]

As shown in the inset of Fig. 6B, the rocking curve of (002) diffraction was measured to study the relation between the crystalline direction and the substrate orientation as well as to obtain the degree of magnetic alignment from distribution of (002) intensity. The crystalline *c* axis appears to be closely aligned with the substrate plane in which the magnetic field was applied during the growth, with a 20-degree FWHM (full width at half maximum) angular dispersion. Rocking scans performed by the 4-circle neutron diffractometer probes the distribution of magnetic moment and (002) orientation and the result agrees very well with the texture-orientation distribution obtained by the in-plane pole figure using X-ray diffraction (ESI S4†).

The hysteresis loops of the hexagonal $Co_{3.3}N$ nanoparticles exhibit substantial coercivities of 0.19 T at 300 K and 0.4 T at 10 K (Fig. 5C). These coercivities indicate appreciable magnetocrystalline anisotropy associated with the noncubic $CdMg_3$-type crystal structure. The anisotropy is further confirmed by measuring the easy- and hard-axis magnetization curves for the aligned nanoparticle sample. The hysteresis loops measured at 10 K along the easy and hard directions for the aligned $Co_{3.3}N$ nanoparticle sample are shown in Fig. 6C. The loops show a comparatively high coercivity B_c = 0.42 T and a high remanence ratio M_r/M_s = 0.80 along the easy axis as compared to the values measured along the hard axis (B_c = 0.14 T and M_r/M_s = 0.24). The room-temperature values along the easy- and hard-axes are B_c = 0.2 T and M_r/M_s = 0.76 and B_c = 0.07 T and M_r/M_s = 0.21, respectively (not shown here). Experimentally, we have estimated the anisotropy constant K_1 from the point where easy- and hard-axis magnetization curves intersect for the aligned nanoparticles. The intersection yields an anisotropy field $B_a = \mu_0 H_a$ = 2.0 T at 10 K and, based on the relation $B_a = 2K_1/M_s$, an anisotropy of 1.01 MJ m^{-3} (10.1 Mergs per cm^3).

The magnetic properties and phase stability of the rhombohedral $Co_{2.8}N$ nanoparticles are provided in the ESI S5.† In brief, the $Co_{2.8}N$ nanoparticles crystallizing in the rhombohedral structure also exhibit appreciable K_1 = 1.04 MJ m^{-3} (10 Mergs per cm^3) and M_s = 580 kA m^{-1} (or J_s = 0.73 T). The underlying anisotropy is also reflected by high coercivity, for example B_c = 0.6 T at 10 K. The temperature dependence of the magnetization indicates a Curie temperature in the vicinity of 450 K. Nanoparticles of this phase show a decomposition above 605 K.

The magnetic anisotropy values for the nanoparticles of the hexagonal $Co_{3.3}N$ (K_1 = 1.01 MJ m^{-3}) and rhombohedral $Co_{2.8}N$ (K_1 = 1.04 MJ m^{-3}) are higher than the anisotropy of bulk hcp Co (0.65 MJ m^{-3})[48] and Co nanoparticles reported in this study (K_1 = 0.55 MJ m^{-3}, not shown here). Note that Co nanoparticles of much smaller sizes of less than 0.68 nm size (15 atoms) deposited on Pt substrate have shown enhanced magnetic anisotropies.[52] These particle sizes are much smaller than the critical super-paramagnetic size (D_{sp}), a quantity related to the thermal stability of nanomagnets, which can be estimated using $K_1 V_{np} = 25 k_B T$.[49] V_{np} and k_B are the volume of the nanoparticles and Boltzmann constant, respectively. Thus, the smaller Co nanoparticles are not thermally stable and expected to show only superparamagnetic behavior at room temperature, which is not desirable for energy and data storage applications. On the other hand, Co nanoparticles with larger particle sizes >1.0 nm only exhibited anisotropy values similar to that of bulk Co.[52–54] For example, hcp Co nanoparticles with an average size of 3 nm exhibit K_1 = 0.49 MJ m^{-3}, similar to that of bulk Co and are superparamagnetic with a blocking temperature of 20 K.[54]

The enhancement of K_1 by the introduction of N atoms in the new Co_3N compounds fundamentally must be understood at the level of the spin-polarized electronic structure. From the viewpoint of crystal structures, the nitrogen in the newly synthesized compounds can be considered as a substitutional atom in the case of the hexagonal phase and an interstitial atom in the case of the rhombohedral phase. It is possible that the N atoms strengthen the spin–orbit coupling of the Co and subsequently increase the magnetic anisotropy energy. By considering the high magnetic anisotropies, the average particle sizes of the nanoparticles of rhombohedral $Co_{2.8}N$ (14.6 nm) and hexagonal $Co_{3.3}N$ (16.4 nm) are expected to be larger than the critical super-paramagnetic size (D_{sp}). For example, we have estimated D_{sp} = 5.9 nm at room temperature for the hexagonal Co_3N nanoparticles.

4. Conclusions

We have used a combined experimental and computational approach to investigate how interstitial and substitutional modification of Co with nitrogen can create new magnetic structures with noteworthy properties. The large difference in formation enthalpy is overcome by the non-equilibrium nanoparticle synthesis, and a high saturation magnetic polarization and an appreciable magnetic anisotropy are found for the $CdMg_3$-ordered $Co_{3.3}N$ nanoparticles. The anisotropy of the hexagonal $Co_{3.3}N$ nanoparticles is in the range of several rare-earth-free permanent-magnet materials that have shown high coercivities and room-temperature energy products upon nanostructuring.[29,55–57] Therefore, they can have potential uses in microelectromechanical systems (MEMS) and also can be used to create future rare-earth-free permanent magnets, if scale-up methods are developed. On the basis of K_1 = 1.01 MJ m^{-3} and J_s = 1.28 T for the hexagonal Co_3N, an energy

product as high as about 318 kJ m^{-3} (≈40 MGOe) might be obtained in principle by appropriate nanostructuring and compaction of these nanoparticles. From the critical materials viewpoint, these new structures do not contain any scarce rare-earth or other expensive elements. The combined experimental and computational approach employed here is not limited to Co–N systems and can be extended to discover new phases in other material systems. A typical example is the family of Heusler alloys in which more than about 90% of the compounds are metastable.[1] The new metastable structures may be useful for future technological applications in areas such as magnetism and catalysis, and this work provides a strategy to accelerate the discovery of new phases for energy, data storage, and spintronics applications.

Conflicts of interest

There are no conflicts to declare.

Author contributions

B.B. and D.J.S. developed the concept and design for the experiments. B.B. carried out the sample preparation and characterization. X.Z., C.-Z.W, and K.-M.H performed the theoretical calculations. S.B. and A.E. contributed towards XPS measurements. A.S., Y.J. and X.Z.L carried out TEM measurements and analysis, and S.R.V contributed towards XRD measurement and analysis. X.X., H.C., and H.W. performed neutron diffraction measurements and analysis. B.B. and D.J.S. analyzed the results and wrote the manuscript. R.S. participated in scientific discussion and commented critically on the manuscript. All authors critically read and commented on the manuscript. D.J.S. supervised the project.

Acknowledgements

Experimental and theoretical works were supported by the National Science Foundation (NSF), Division of Materials Research (DMR), under the awards DMREF: SusChEM 1436385 and 1436386, respectively. Research at Nebraska was performed in part in the Nebraska Nanoscale Facility, Nebraska Center for Materials and Nanoscience, which is supported by the NSF under Award NNCI: 1542182, and the Nebraska Research Initiative (NRI). The work at ORNL's HFIR was sponsored by the Scientific User Facilities Division, Office of Science, Basic Energy Sciences, U.S. Department of Energy. The development of adaptive genetic algorithm (AGA) method was supported by the US Department of Energy, Basic Energy Sciences, Division of Materials Science and Engineering, under Contract No. DE-AC02-07CH11358, including a grant of computer time at the National Energy Research Scientific Computing Center (NERSC) in Berkeley, CA. Authors thank Z. Sun and B. Das for technical assistance and helpful discussions.

References

1 S. Sanvito, C. Oses, J. Xue, A. Tiwari, M. Zic, T. Archer, P. Tozman, M. Venkatesan, M. Coey and S. Curtarolo, *Sci. Adv.*, 2017, **3**, e1602241.
2 C. Collins, M. S. Dyer, M. J. Pitcher, G. F. S. Whitehead, M. Zanella, P. Mandal, J. B. Claridge, G. R. Darling and M. J. Rosseinsky, *Nature*, 2017, **546**, 280–284.
3 E. M. Vogel, *Nat. Nanotechnol.*, 2007, **2**, 25–32.
4 J. Wood, *Mater. Today*, 2008, **11**, 40–44.
5 K. Strnat, G. Hoffer, J. Olson and W. Ostertag, *J. Appl. Phys.*, 1967, **38**, 1001–1002.
6 M. Sagawa, S. Fujimura, N. Togawa, H. Yamamoto and Y. Matsuura, *J. Appl. Phys.*, 1984, **55**, 2083–2087.
7 M. Takahashi, H. Shoji, H. Takahashi, H. Nashi and T. Wakiyama, *J. Appl. Phys.*, 1994, **76**, 6642–6647.
8 R. Skomski and D. J. Sellmyer, *J. Rare Earths*, 2009, **27**, 675–679.
9 J. M. D. Coey and H. Sun, *J. Magn. Magn. Mater.*, 1990, **87**, L251–L254.
10 R. Skomski, "Interstitial modification", in *Rare-Earth—Iron Permanent Magnets*, ed. J. M. D. Coey, University Press, Oxford, 1996, pp. 178–217.
11 M. Widenmyer, L. Shlyk, N. Becker, R. Dronskowski, E. Meissner and R. Niewa, *Eur. J. Inorg. Chem.*, 2016, **2016**, 4792–4801.
12 M. B. Lourenco, M. D. Carvalho, P. Fonseca, T. Gasche, G. Evans and M. Godinho, *J. Alloys Compd.*, 2014, **612**, 176–182.
13 K. Suzuki, T. Kaneko, H. Yoshida, H. Morita and H. Fujimori, *J. Alloys Compd.*, 1995, **224**, 232–236.
14 B. Balasubramanian, P. Manchanda, R. Skomski, P. Mukherjee, S. R. Valloppilly, B. Das, G. C. Hadjipanayis and D. J. Sellmyer, *Appl. Phys. Lett.*, 2016, **108**, 152406.
15 D. Y. Feng, Z. W. Liu, Z. G. Zheng, D. C. Zeng and G. Q. Zhang, *J. Magn. Magn. Mater.*, 2013, **347**, 18–25.
16 A. M. Gabay and G. C. Hadjipanayis, *J. Alloys Compd.*, 2016, **657**, 133–137.
17 Z. D. Zhang, W. Liu, J. P. Liu and D. J. Sellmyer, *J. Phys. D: Appl. Phys.*, 2000, **33**, R217–R246.
18 N. Nosengo, *Nature*, 2016, **533**, 23–25.
19 P. Raccuglia, K. C. Elbert, P. D. F. Adler, C. Falk, M. B. Wenny, A. Mollo, M. Zeller, S. A. Friedler, J. Schrier and A. J. Norquist, *Nature*, 2016, **533**, 73–76.
20 A. Jain, Y. Shin and K. A. Persson, *Nat. Rev.*, 2016, **1**, 15004.
21 C.-K. Skylaris, *Science*, 2016, **351**, 1394–1396.
22 K. Lejaeghere, *et al.*, *Science*, 2016, **351**, aad3000.
23 S. Curtarolo, G. L. W. Hart, M. B. Nardelli, N. Mingo, S. Sanvito and O. Levy, *Nat. Mater.*, 2013, **12**, 191–201.
24 W. Sun, A. Holder, B. Orvannos, E. Arca, A. Zakutayev, S. Lany and G. Ceder, *Chem. Mater.*, 2017, **29**, 6936–6946.
25 P. Zhou, L. Jiang, F. Wang, K. Deng, K. Lv and Z. Zhang, *Sci. Adv.*, 2017, **3**, e1601945.
26 J. C. Crowhurst, A. F. Goncharov, B. Sadigh, C. L. Evans, P. G. Morrall, J. L. Ferreira and A. J. Nelson, *Science*, 2006, **311**, 1275–1278.

27 A. F. Young, C. Sanloup, E. Gregoryanz, S. Scandolo, R. J. Hemley and H.-K. Mao, *Phys. Rev. Lett.*, 2006, **96**, 155501.
28 X. Zhao, L. Ke, C.-Z. Wang and K.-M. Ho, *Phys. Chem. Chem. Phys.*, 2016, **18**, 31680–31690.
29 B. Balasubramanian, P. Mukherjee, R. Skomski, P. Manchanda, B. Das and D. J. Sellmyer, *Sci. Rep.*, 2014, **4**, 6265.
30 V. G. Harris, Y. Chen, A. Yang, S. Yoon, Z. Chen, A. L. Geiler, J. Gao, C. N. Chinnasamy, L. H. Lewis, C. Vittoria, E. E. Carpenter, K. J. Carrol, R. Goswami, M. A. W. Willard, L. Kurihara, M. Gjoka and O. Kalogirou, *J. Phys. D: Appl. Phys.*, 2010, **43**, 165003.
31 M. Zamanpour, S. Bennet, P. Taheri, Y. Chen and V. H. Harris, *J. Appl. Phys.*, 2014, **115**, 17A747.
32 A. A. El-Gendy, M. Qian, Z. J. Huba, S. N. Khanna and E. E. Carpenter, *Appl. Phys. Lett.*, 2014, **104**, 023111.
33 (*a*) X. Zhao, M. C. Nguyen, W. Y. Zhang, C. Z. Wang, M. J. Kramer, D. J. Sellmyer, X. Z. Li, F. Zhang, L. Q. Ke, V. P. Antropov and K.-M. Ho, *Phys. Rev. Lett.*, 2014, **112**, 045502; (*b*) S. Wu, M. Ji, C. Z. Wang, M. C. Nguyen, X. Zhao, K. Umemoto, R. M. Wentzcovitch and K. M. Ho, *J. Phys.: Condens. Matter*, 2014, **26**, 035402.
34 H. Okamoto, *Phase diagram for Binary Alloys*, ASM, Materials Park, 2000, p. 252.
35 D. M. Deaven and K. M. Ho, *Phys. Rev. Lett.*, 1995, **75**, 288–291.
36 J. D. Fast, *Gases in metals*, Macmillan, London, 1976.
37 Y.-J. Zhang, Q. Yao, Y. Zhang, T.-Y. Cui, D. Li, W. Liu, W. Lawrence and Z.-D. Zhang, *Cryst. Growth Des.*, 2008, **8**, 3206–3212.
38 K. S. Rao, T. Balajia, Y. Lingappas, M. R. P. Reddy and T. L. Prakash, *J. Exp. Nanosci.*, 2013, **8**, 162–170.
39 R. Goyal, S. Lamba and S. Annapoorni, *Phys. Status Solidi A*, 2016, **213**, 1309–1316.
40 N. Arora and B. R. Jagirdar, *J. Mater. Chem.*, 2012, **22**, 20671–20679.
41 X. Q. Zhao, S. Veintemillas-Verdaguer, O. Bomati-Miguel, M. P. Morales and H. B. Xu, *Phys. Rev. B: Condens. Matter Mater. Phys.*, 2005, **1**, 024106.
42 (*a*) X. Z. Li, *Ultramicroscopy*, 2010, **110**, 297–304; (*b*) X. Z. Li, *Microsc. Microanal.*, 2016, **22**(Suppl. 3), 564–565.
43 R. Gupta, N. Pandey, A. Tayal and M. Gupta, *AIP Adv.*, 2015, **5**, 097131.
44 (*a*) B. Balasubramanian, P. Manchanda, R. Skomski, P. Mukherjee, B. Das, T. A. George, G. C. Hadjipanayis and D. J. Sellmyer, *Appl. Phys. Lett.*, 2015, **106**, 242401; (*b*) B. Balamurugan, B. Das, V. R. Shah, R. Skomski, X. Z. Li and D. J. Sellmyer, *Appl. Phys. Lett.*, 2012, **101**, 122407.
45 S. Yu, B. Huang, X. Jia, Q. Zeng, A. R. Oganov, L. Zhang and G. Frapper, *J. Phys. Chem. C*, 2016, **120**, 11060–11067.
46 S. Wang, *et al.*, *J. Am. Chem. Soc.*, 2015, **137**, 4815–4822.
47 (*a*) G. V. Vajenine, *Inorg. Chem.*, 2007, **46**, 5146–5148; (*b*) B. Balamurugan and T. Maruyama, *Appl. Phys. Lett.*, 2006, **89**, 033112.
48 C. M. Caskey, R. M. Richards, D. S. Ginley and A. Zakutayev, *Mater. Horiz.*, 2014, **1**, 424.
49 R. Skomski, *J. Phys.: Condens. Matter*, 2003, **15**, R841–R896.
50 V. F. Sears, *Neutron News*, 1992, **3**, 26–37.
51 X. Xu, X. Zhang, Y. Yin, B. Balasubramanian, B. Das, Y. Liu, A. Hug and D. J. Sellmyer, *J. Phys. D: Appl. Phys.*, 2017, **50**, 25002.
52 P. Gambardella, S. Rusponi, M. Veronese, S. S. Dhesi, C. Grazioli, A. Dallmeyer, I. Cabria, R. Zeller, P. H. Dederichs, K. Kern, C. Carbone and H. Brune, *Science*, 2003, **300**, 1130–1133.
53 A. Tamion, C. Raufast, M. Hillenkamp, E. Bonet, J. Jouanguy, B. Canut, E. Bernstein, O. Boisron, W. Wernsdorfer and V. Dupuis, *Phys. Rev. B: Condens. Matter Mater. Phys.*, 2010, **81**, 144403.
54 (*a*) C. B. Murray, S. Sun, H. Doyle and T. Betley, *MRS Bull.*, 2001, 985; (*b*) D. V. Talapin, E. V. Shevchenko and H. Weller, "Synthesis and Characterization of Magnetic Nanoparticles", in *Nanoparticles – From Theory to Application*, ed. G. Schmid, Wiley, Germany, 2005, pp. 178–217.
55 B. Balasubramanian, B. Das, R. Skomski, W. Y. Zhang and D. J. Sellmyer, *Adv. Mater.*, 2013, **13**, 6090–6093.
56 M. A. McGuire and O. Rios, *J. Appl. Phys.*, 2015, **117**, 053912.
57 T. R. Gao, *et al.*, *Phys. Rev. B*, 2016, **94**, 060411(R).